Ionics (2023) 29:1507–1514
https://doi.org/10.1007/s11581-023-04901-7

ORIGINAL PAPER

Perovskite-type $Nd_{0.75}Ba_{0.25}Co_{0.8}Fe_{0.2}O_{3-\delta}$ cathode for intermediate temperature solid oxide fuel cells

Daniel Sikstrom[1] · Aroosa Javed[1] · Shoaib Muhammad[1] · Venkataraman Thangadurai[1]

Received: 16 August 2022 / Revised: 27 December 2022 / Accepted: 23 January 2023 / Published online: 7 February 2023

Abstract

Perovskite-type $Nd_{0.75}Ba_{0.25}Co_{0.8}Fe_{0.2}O_{3-\delta}$ (NBCF25) was prepared via solid-state synthesis method at 1300 °C in air. Powder X-ray diffraction showed the formation of a single-phase orthorhombic phase in the *Pnma* space group. It showed minor reactivity with Sr and Mg-co-doped lanthanum gallate (LSGM) when sintered with 30 wt.% LSGM at 1050 °C. 4-probe DC chronopotentiometry measurements were performed on the sintered sample pellets and showed a maximum conductivity of 674 S/cm at 700 °C. 2-probe AC electrochemical impedance spectroscopy measurements were performed on LSGM pellets from 650 to 800 °C to investigate the oxygen reduction property of NBCF25 using a composite slurry (70 wt.% NBCF and 30 wt.% LSGM). It showed the lowest area-specific resistance of 0.07 Ω cm^2 at 800 °C in air. Impedance spectroscopy genetic programming was used to understand the oxygen reduction reaction.

Keywords Perovskite · Cathode · Oxygen reduction reaction · Impedance spectroscopy · SOFCs

Introduction

As the world's population continues to increase, the energy required to power it increases as well [1]. To keep up with the ever-growing energy demand, larger amounts of fossil fuels are being used each year causing the global emissions of CO_2 to increase at an unsustainable rate [2, 3]. For the world to maintain the current energy demand while also reducing CO_2 emissions, the development of carbon–neutral energy sources is crucial. Solid oxide fuel cells (SOFCs) are a promising source of carbon–neutral energy due to their high chemical-to-electrical energy conversion process that does not produce the harmful pollutants (when hydrogen is used as a fuel) associated with combustion reactions [4]. Apart from hydrogen, SOFCs can also use other fuels such as methane, carbon monoxide, and other hydrocarbons due to the higher operating temperature compared to other fuel cells, including proton exchange membrane fuel cells and direct methanol fuel cells [5]. SOFCs commonly operate at a high temperature ranging from 800 to 1000 °C. However, at these temperatures, long-term cell degradation is an issue as the components that are in contact with each other will react and form less conductive products [6]. Thus, it is important to lower the operating temperature of these cells to an intermediate temperature (IT) range (400–800 °C) to increase their lifespan and limit the drop in efficiency over time. However, at these lower temperatures, the kinetics for the oxygen reduction (ORR) at the cathode are slow; therefore, advanced cathodes with high catalytic activity for the ORR must be developed [7, 8].

Recent studies have focused on improving the performance of various mixed ionic-electronic conducting metal oxide perovskites for SOFCs. Extensive research has been done on the optimization of $La_{0.6}Sr_{0.4}Co_{0.2}Fe_{0.8}O_{3-\delta}$ (LSCF) cathodes due to their high total electrical conductivity and high electrochemical activity towards the ORR. However, LSCF has shown durability issues mainly caused by electrode poisoning leading to degradation of the LSCF cathode [9]. LSCF has also been shown to react with the $La_{0.8}Sr_{0.2}Ga_{0.8}Mg_{0.2}O_{3-\delta}$ (LSGM) electrolyte which lowers the performance of the cell [10]. Our group found better compatibility with the LSGM electrolyte by replacing La in LSCF with Nd and changing the stoichiometry to $Nd_{0.75}Sr_{0.25}Co_{0.8}Fe_{0.2}O_{3-\delta}$ (NSCF). The better compatibility is attributed to a lower thermal expansion coefficient (TEC) that is closer to the TEC of LSGM and no reactivity between NSCF and LSGM [11]. Substituting an A-site ion for one

✉ Venkataraman Thangadurai
vthangad@ucalgary.ca
https://ucalgary.ca/thangadurai-group

[1] Department of Chemistry, University of Calgary, 2500 University Dr NW, Calgary T2N 1N4, Canada

with a larger ionic radius increases the free lattice volume allowing for greater oxygen diffusion and transport through oxygen vacancies. Thus, we were curious about the effect of replacing Sr with Ba in $Nd_{0.75}Sr_{0.25}Co_{0.8}Fe_{0.2}O_{3-\delta}$ [12]. A similar $NdBaCoFeO_{5+\delta}$ double perovskite has been studied previously, but the single perovskite variation has not been looked at so far [13]. In this paper, a new Nd-based $Nd_{0.75}Ba_{0.25}Co_{0.8}Fe_{0.2}O_{3-\delta}$ (NBCF25) perovskite is synthesized using a high temperature, solid-state reaction, and the phase formation, electrical conductivity from 100 to 800 °C, ASR from 650 to 800 °C, and the rate-limiting step of the ORR from 650 to 800 °C is determined.

Experimental aspects

Material synthesis

The perovskite-type $Nd_{0.75}Ba_{0.25}Co_{0.8}Fe_{0.2}O_{3-\delta}$ was prepared by a solid-state reaction in air at an elevated temperature. Neodymium oxide (Nd_2O_3) (99.9% Sigma-Aldrich), barium carbonate ($BaCO_3$) (99.9% Alfa Aesar), cobalt oxide (Co_3O_4) (99% Alfa Aesar), and iron oxide (Fe_2O_3) (99 + % Sigma-Aldrich) were mixed in required stoichiometric quantities. The precursors were ball milled with isopropanol for 3 h followed by calcination at 900 °C for 15 h in air. The calcined samples were ball milled again for 3 h to reduce the particle size and then pressed into circular pellets (diameter of ≈ 1.2 cm and length of ≈ 1 cm). The pellets were sintered at 1300 °C for 10 h in air. Finally, the pellets were crushed, and ball milled for 3 h followed by sintering to give a fine powder. $La_{0.8}Sr_{0.2}Ga_{0.8}Mg_{0.2}O_{3-\delta}$ (LSGM) was obtained from fuelcellmaterials, a Nexceris company, USA, and pressed into circular pellets (≈ 0.5 mm in thickness and ≈ 10 mm in diameter) and sintered at 1350 °C for 8 h.

Phase characterization

Powder X-ray diffraction (PXRD) measurements of the as-prepared samples were obtained using a Rigaku SmartLab® diffractometer (CuKα radiation, $\lambda_{K\alpha1} = 1.540593$ Å, $\lambda_{K\alpha2} = 1.544414$ Å; 40 kV and 50 mA; 0.01° steps, 0.5°/min). The powder samples were packed into an aluminum well with a depth of 0.3 mm to increase the signal-to-noise ratio. An X-ray fluorescence reduction mode was used on the detector (Rigaku HYPIX-3000 detector in 1-D mode). The incident slit was set to 0.5° with an incident mask of 10 mm. The receiving optics was set at 20 mm. A 2.5° solar slit was used on both the incident and receiving sides. A CuKβ filter was used to remove the Kβ radiation, and an X-ray anti-scattering device was also used to limit background radiation. The samples were spun at 60 rpm for averaging data.

4-probe DC chronopotentiometry measurements

4-probe DC chronopotentiometry measurements were performed on the sintered sample pellets (diameter of ≈ 1.2 cm and length of ≈ 1 cm) using a BioLogic VSP-300 potentiostat. Groves were cut into the sample pellet and Au wires were wrapped around these grooves to create the inner probes where the potential is measured. The sides of the pellets were coated with gold which served as a current collector. A constant current (0.1–0.35 A) was applied on the sides and the resulting voltage was measured. The following equation was used to calculate the conductivity where I is current (A), V is potential (V), L is the length between the inner probes (cm), and A is the area of the outer probes [14] (cm^2):

$$\sigma = \frac{I}{V} \times \frac{L}{A} \tag{1}$$

Microstructural analysis

The microstructure was measured by scanning electron microscopy (SEM) with a field emission gun (ZEISS Sigma) operating at an accelerated voltage of 10 kV, a working distance of 6.7 mm, and 10^4 times magnification.

Electrochemical impedance spectroscopy measurements (EIS)

A VersaSTAT 3 potentiostat and galvanostat was used to perform the EIS measurements using alternating current (AC) with an amplitude of 10 mV over a frequency range of 10^{-1}–10^6 Hz in air. These symmetric cells were prepared by screen printing a composite slurry (70 wt.% NBCF25 and 30 wt.% LSGM) onto an LSGM pellet (≈ 0.5 mm in thickness and ≈ 10 mm in diameter) and then sintering the pellet at 1050 °C for 5 h. These pellets were coated with gold which served as a current collector.

Impedance spectroscopy genetic programming (ISGP)

ISGP was used to generate a distribution function of relaxation times (DFRT), a model that represents different processes as peaks in the time domain [15–17]. ISGP utilizes the following equation to generate a Nyquist plot based on the DFRT that best fits the measured [18] impedance data:

$$Z(\omega) = R_\infty + R_{pol} \int_{-\infty}^{\infty} \frac{\Gamma(\log(\tau))}{1 + i\omega\tau} d(\log(\tau)) \tag{2}$$

where Z is the impedance, R_∞ is the series resistance, R_{pol} is the total polarization resistance, Γ is the DFRT, τ is the relaxation time, and ω is the angular frequency. The ISGP

program will generate several DFRT models and grade them based on a "fitness function" based on its compatibility with the experimental impedance data; the model with the highest grade will be used for generation 1. The next generation will be an evolution of the previous generation with minor changes to the DFRT ("mutation") and these new models are again ranked and the model with the highest grade is used to produce the next generation. The program reaches its final model when all mutations of the current model result in a lower grade [19].

Results and discussion

Phase characterization

Powder X-ray diffraction refinement of NBCF25 shows the formation of a single-phase orthorhombic phase in the *Pnma* space group (Fig. 1). The quality of the refinement is supported by a weighted reliability factor (R_{wp}) of 7.3% and a chi-squared (χ^2) of 1.13. The A-site occupies the 4c Wyckoff position and is made up of 75% Nd and 25% Ba. The B-site occupies the 4b Wyckoff positive and is made up of 80% Co and 20% Fe. There are two types of oxygen sites one occupying the 4c Wyckoff position and the other occupying the 8d Wyckoff position. Figure 2 shows the crystal structure of $Nd_{0.75}Ba_{0.25}Co_{0.8}Fe_{0.2}O_{3-\delta}$.

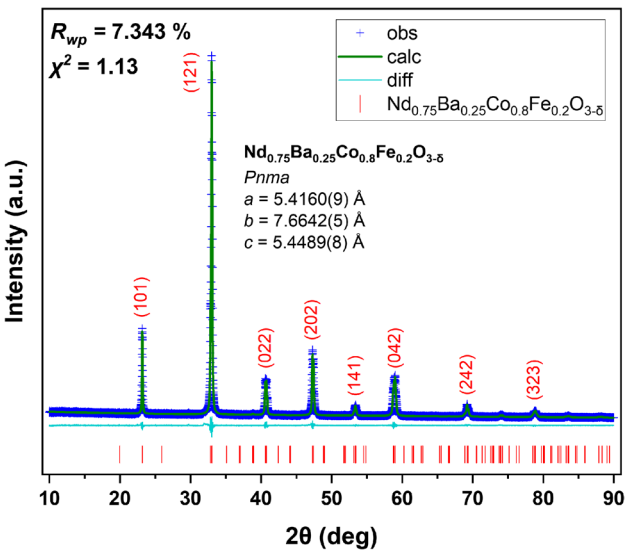

Fig. 1 PXRD Rietveld refinement profile for $Nd_{0.75}Ba_{0.25}Co_{0.8}Fe_{0.2}O_{3-\delta}$. Details of refinement results are provided in. Table 1 [20]

DC electrical conductivity

The electrical conductivity as a function of temperature as well as the TGA curve for NBCF25 is shown in Fig. 3. NBCF25 is a p-type semiconductor. The conductivity trends can be broken down into 5 different regions. In the first region from 100 to 300 °C, there is an increase in conductivity as temperature increases; there is also a slight weight loss associated desorption of atmospheric H_2O and CO_2. In the second region from 300 to 400 °C, there is a sudden drop in conductivity and a sudden weight loss associated with the reduction of the B-site ions (Fe^{4+}/Co^{4+}) and the loss of oxygen as shown in the forward reaction of Eq. 3; this suggests the formation of $B_B^X - O_O^X - B_B^X$ and $B_B^X - V_O^{\bullet\bullet} - B_B^X$ which block the transport of electrons where B_B^X is Fe^{3+} or Co^{3+} sitting at the Fe^{3+} or Co^{3+} site respectively, O_O^X is oxygen sitting at the oxygen site, $V_O^{\bullet\bullet}$ is a vacancy at the O^{2-} site, and $B_B^{\bullet}$ is Fe^{4+} or Co^{4+} sitting at the Fe^{3+} or Co^{3+} site respectively. [22] In the third region from 400 to 500 °C, there is a sudden increase in conductivity and a sudden weight gain which is associated with the oxidation of the previously reduced B-site ions (Fe^{3+}/Co^{3+}) and the re-absorption of oxygen as shown in the reverse reaction of Eq. 2. In the fourth region from 500 to 700 °C, there is a rapid loss of weight but unlike region 2, the conductivity increases indicating semiconducting behavior. The fifth region from 700 to 800 °C has the same trend as the second region.

$$2B_B^{\bullet} + O_O^X \leftrightarrows 2B_B^X + V_O^{\bullet\bullet} + \frac{1}{2}O_2 \quad (3)$$

Chemical reactivity with LSGM

Figure 4 shows the PXRD measurements for the LSGM electrolyte, the as-prepared NBCF25, 70% NBCF25 mixed with 30% LSGM, and 70% NBCF25 sintered with 30%

Table 1 The powder X-ray refinement results for $Nd_{0.75}Ba_{0.25}Co_{0.8}Fe_{0.2}O_{3-\delta}$ (R_{wp} = 7.343%; χ^2 = 1.13; phase $Nd_{0.75}Ba_{0.25}Co_{0.8}Fe_{0.2}O_{3-\delta}$: space group = *Pnma*, *a* = 5.4160(9) Å, *b* = 7.6642(5) Å, *c* = 5.4489(8) Å). Occupancy parameters are not refined

Atom	Wyckoff-site	*x/a*	*y/b*	*z/c*	Occupancy	U_{iso} (Å^2)
Nd^{3+}/Ba^{2+}	4c	0	0.25	0	0.75/0.25	0.08
Co^{3+}/Fe^{3+}	4b	0	0	0.5	0.8/0.2	0.07
O^{2-}	4c	0.503	0.25	0.0452	1	0.05
O^{2-}	8d	0.301	0.0156	0.741	1	0.06

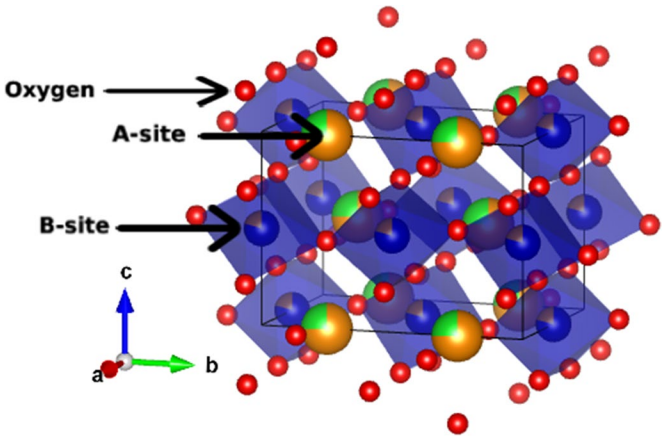

Fig. 2 The crystal structure of $Nd_{0.75}Ba_{0.25}Co_{0.8}Fe_{0.2}O_{3-\delta}$ determined using Rietveld refinement. 3D rendering generated by VESTA 3. [21] A-site consists of 75% Nd and 25% Ba. B-site consists of 80% Co and 20% Fe

LSGM at 1050 °C. A new peak arises at $2\theta = 30.08°$ which indicates the reaction between NBCF25 and LSGM forming $BaLaGa_3O_7$ or $BaNdGa_3O_7$ [23]. Despite the reactivity, the area specific resistance of a LSGM-NBCF25 symmetric cell is low (Fig. 5) and SEM image (Fig. 6) of the cross-section shows good contact between LSGM and NBCF25 indicating that the formation of $BaLaGa_3O_7$ or $BaNdGa_3O_7$ has little effect on the performance of NBCF25 when used with LSGM.

Area specific resistance (ASR)

Figure 6 shows a cross-sectional SEM image of an NBCF25 symmetric cell with a porous cathode layer and a dense LSGM electrolyte. The strong contact between NBCF25 and LSGM indicates good surface compatibility when sintered at 1050 °C. The area-specific resistance of a symmetric NBCF25 cell at various intermediate temperatures (650 °C to 800 °C) is shown in Fig. 5A. The ASR values are 0.49, 0.2, 0.11, and 0.07 Ω cm^2 at 650 °C, 700 °C, 750 °C, and 800 °C respectively. Thus, NBCF25 has high catalytic activity towards the ORR at 750 °C and 800 °C which is determined through its low ASR at these temperatures (≈ 0.1 Ω cm^2). Figure 5B shows the DFRT plot for NBCF25 with the inductance and series resistance removed where each peak corresponds to the frequency (*f*) of an individual electrical process which mimics a resistor (*R*) and a constant phase element (CPE) in parrel, known as an RC element. The area under each curve in the DFRT plot corresponds to the percentage of the total ASR that

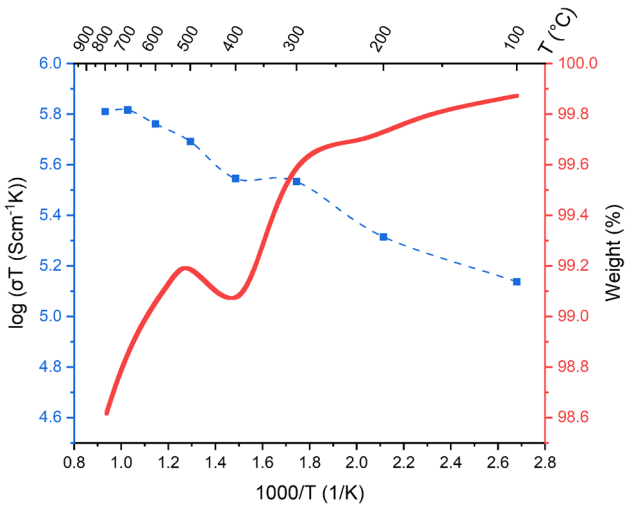

Fig. 3 Arrhenius plot of the electrical conductivity for $Nd_{0.75}Ba_{0.25}Co_{0.8}Fe_{0.2}O_{3-\delta}$ in air (blue) and TGA in N_2 (red)

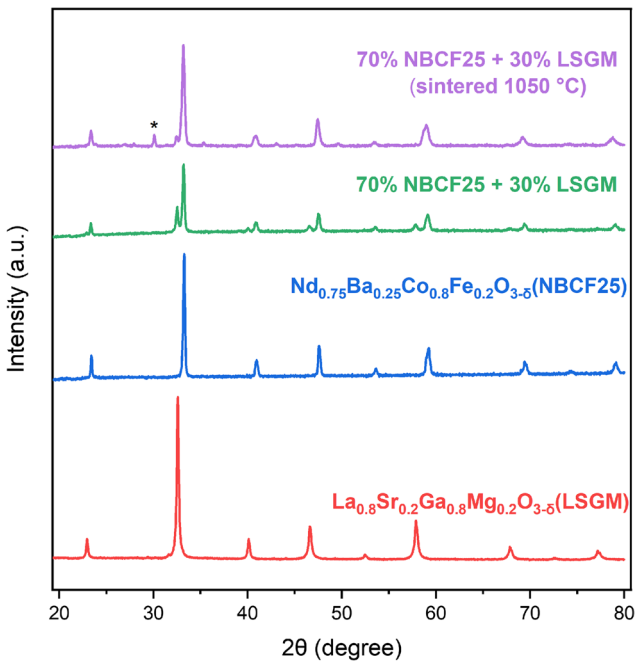

Fig. 4 PXRD of $La_{0.8}Sr_{0.2}Ga_{0.8}Mg_{0.2}O_{3-\delta}$ (LSGM); $Nd_{0.75}Ba_{0.25}Co_{0.8}Fe_{0.2}O_{3-\delta}$ (NBCF25), a composite of 70% NBCF25 and 30% LSGM, and a composite of 70% NBCF25 and 30% LSGM sintered at 1050 °C for 5 h. $BaLaGa_3O_7$ or $BaNdGa_3O_7$ (*)

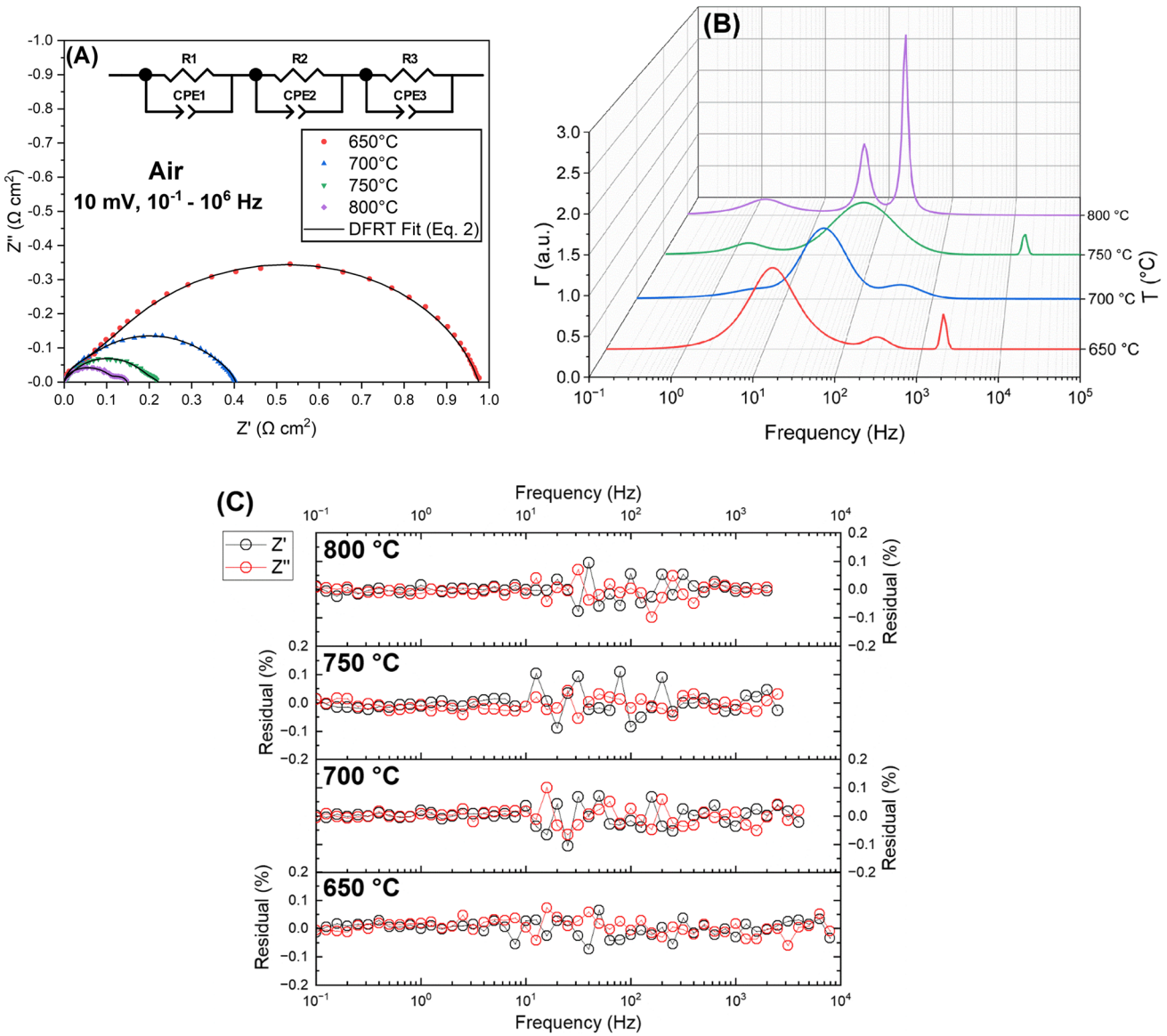

Fig. 5 **A** Nyquist plot of a symmetrical cell with a composite electrode (70% $Nd_{0.75}Ba_{0.25}Co_{0.8}Fe_{0.2}O_{3-\delta}$ + 30% LSGM) using LSGM with a thickness of 0.5 mm as an electrolyte where the ASR is equal to half the diameter of the arcs. The solid lines on the graph are generated from the equivalent circuit model given by Eq. 2. Measurements are taken at 650 °C to 800 °C in air. Corrected for cathode area. Inductance and series resistance is removed. **B** DFRT model of a Nyquist plot for $Nd_{0.75}Ba_{0.25}Co_{0.8}Fe_{0.2}O_{3-\delta}$ where each peak corresponds to an arc on the Nyquist plot. **C** Linear Kramers–Kronig validity test performed on Nyquist data at 650 to 800 °C. The high-frequency inductance was removed at all temperatures

is due to the resistance of that electrical process. Then, as the frequency and resistance of the RC element are known, the following formula can be used to calculate [19] capacitance (C):

$$C = \frac{1}{2\pi Rf} \tag{4}$$

which is related to CPE [24]. At 650, 700, and 800 °C, there are two medium-frequency peaks associated with the coupled dissociative adsorption or surface exchange of oxygen and one low-frequency peak associated with oxygen diffusion inside the cathode [25, 26]. At 650 °C, the total resistance is dominated by oxygen diffusion inside the cathode (≈ 91%) (Table 2). At 700 °C, the total resistance becomes dominated by the coupled dissociative

Fig. 6 Cross-sectional SEM images of $Nd_{0.75}Ba_{0.25}Co_{0.8}Fe_{0.2}O_{3-\delta}$ (NBCF25)/$La_{0.8}Sr_{0.2}Ga_{0.8}Mg_{0.2}O_{3-\delta}$ (LSGM) composite cathode screen printed onto LSGM electrolyte

adsorption or surface exchange of oxygen (≈ 70%). At 800 °C, the coupled dissociative adsorption or surface exchange of oxygen and oxygen diffusion inside the cathode contribute equally to the total resistance. At 750 °C, there is one high-frequency peak associated with ion transfer from the cathode to the electrolyte, one medium-frequency, and one low-frequency peak [26]. The total resistance at 750 °C is dominated by coupled dissociative adsorption or surface exchange of oxygen. While contributing very little to the total resistance at 750 °C, the high-frequency charge transfer peak indicates minor instability between NBCF25 and LSGM at this temperature.

The quality of the data used for the ISGP fitting was confirmed using a linear Kramers–Kronig validity test (Fig. 5C) [27–29] (http://www.Iwe.Kit.Edu/Lin-KK.Php). All data points on the Z′ and Z″ axis are within 0.1% of their expected value according to the formula [27]:

$$\Delta_{Z'} = \frac{Z' - Z'_{KK}}{Z'_{KK}} \text{or} \Delta_{Z''} = \frac{Z'' - Z''_{KK}}{Z''_{KK}} \quad (5)$$

where $\Delta_{Z'}$ and $\Delta_{Z''}$ are the residuals for the real and imaginary axis respectively, Z' and Z'' are the experimentally determined real and imaginary values respectively, and Z'_{KK} and Z''_{KK} are the expected real and imaginary values respectively determined from the Kramers–Kronig relations. The residuals all being near or less than 0.1% indicate the data is of very high quality [30, 31].

Table 3 shows a comparison between NBCF25 and various literature perovskite and double perovskite-type cathode materials for IT-SOFCs. NBCF25 has a comparable ASR to $NdBaCoFeO_{5+\delta}$ and $La_{0.6}Sr_{0.4}Co_{0.2}Fe_{0.8}O_{3-\delta}$ (≈ 0.1 Ω cm^2 at 750 °C) [13, 32]. It has a very high electrical conductivity when compared to other perovskites (674 S/cm at 700 °C), 9 times more conductive than $NdBaCoFeO_{5+\delta}$ and 3 times more conductive than $La_{0.6}Sr_{0.4}Co_{0.2}Fe_{0.8}O_{3-\delta}$ [13, 33].

Table 3 Summary of the conductivity and ASR of NBCF and various literature perovskite and double perovskite-type cathode materials for IT-SOFCs

Cathode material	Conductivity (S/cm) (700 °C)	ASR (Ω cm^2) (750 °C)
$Nd_{0.75}Ba_{0.25}Co_{0.8}Fe_{0.2}O_{3-\delta}$	674	0.11 (present study)
$La_{0.6}Sr_{0.4}Co_{0.2}Fe_{0.8}O_{3-\delta}$	200 [33]	0.108 [32]
$La_{0.8}Sr_{0.2}Fe_{0.8}Cu_{0.3}O_{3-\delta}$	182 [34]	0.25 [34]
$Ba_{0.5}Sr_{0.5}Co_{0.8}Fe_{0.2}O_{3-\delta}$	15 [33]	0.01 [35]
$Ba_{0.9}Sr_{0.1}Co_{0.9}In_{0.1}O_{3-\delta}$	12 [36]	0.046 [36]
$Bi_{0.5}Sr_{0.5}Fe_{0.8}Co_{0.2}O_{3-\delta}$	25 [37]	0.052 [37]
$SrCo_{0.95}Ti_{0.05}O_{3-\delta}$	113 [38]	0.0575 [38]
$SrCo_{0.97}V_{0.03}O_{3-\delta}$	113 [38]	0.095 [38]
$SrNd_{0.1}Co_{0.9}O_{3-\delta}$	180 [39]	0.049 [39]
$PrBaCoFeO_{5+\delta}$	163 [13]	0.098 [13]
$NdBaCoFeO_{5+\delta}$	75 [13]	0.119 [13]

Conclusions

In summary, perovskite-type $Nd_{0.75}Ba_{0.25}Co_{0.8}Fe_{0.2}O_{3-\delta}$ (NBCF25) was prepared via solid-state synthesis method at 1300 °C in air. Powder X-ray diffraction showed the formation of a single-phase $Nd_{0.75}Ba_{0.25}Co_{0.8}Fe_{0.2}O_{3-\delta}$ phase in the *Pnma* space group. NBCF25 shows minor reactivity with SrO/MgO-doped lanthanum gallate (LSGM) when sintered with 30% LSGM at 1050 °C. The conductivity of NBCF25 was determined using 4-probe DC chronopotentiometry

Table 2 Calculated capacity and resistance of all RC elements from DFRT of NBCF25

	R1 (Ω cm^2)	C1 (F)	f1 (Hz)	R2 (Ω cm^2)	C2 (F)	f2 (Hz)	R3 (Ω cm^2)	C3 (F)	f3 (Hz)	ASR (Ω cm^2)
650 °C	0.038	0.0023	1.9×10^3	0.046	0.013	2.7×10^2	0.89	0.014	1.3	0.49
700 °C	0.049	0.0086	3.8×10^2	0.28	0.016	3.4×10^1	0.072	0.50	4.1	0.2
750 °C	0.0057	0.0018	1.6×10^4	0.18	0.012	7.8×10^1	0.036	2.64	1.7	0.11
800 °C	0.063	0.012	2.1×10^2	0.049	0.068	5.1×10^1	0.036	2.23	1.5	0.07

on the sintered sample pellets and showed a maximum conductivity of 674 S/cm at 700 °C. The area-specific resistance (ASR) was determined using 2-probe AC electrochemical impedance spectroscopy on LSGM pellets with a screen-printed composite slurry (70 wt.% NBCF25 and 30 wt.% LSGM) and showed a minimum ASR of 0.07 Ω cm^2 at 800 °C.

Acknowledgements One of us (D.S.) thanks the University of Calgary for the PURE (Program for Undergraduate Research Experience) scholarship. The authors would like to thank Bryan Zanza of the Dr. Michelle Dolgos research group at the University of Calgary for the PXRD data used in the phase characterization.

Funding The Natural Sciences and Engineering Research Council of Canada (NSERC) has supported this work through discovery grants to one of us (V. T.) (Award number: RGPIN-2021–02493).

Declarations

Conflict of interest The authors declare no competing interests.

References

1. Jiang C, Ma J, Corre G, Jain SL, Irvine JTS (2017) Challenges in Developing Direct Carbon Fuel Cells. Chem Soc Rev 46(10):2889–2912. https://doi.org/10.1039/C6CS00784H
2. Gür TM (2018) Review of Electrical Energy Storage Technologies, Materials and Systems: Challenges and Prospects for Large-Scale Grid Storage. Energy Environ Sci 11(10):2696–2767. https://doi.org/10.1039/C8EE01419A
3. Wang H, Liang X, Wang J, Jiao S, Xue D (2020) Multifunctional Inorganic Nanomaterials for Energy Applications. Nanoscale 12(1):14–42. https://doi.org/10.1039/C9NR07008G
4. Singh P, Minh NQ (2005) Solid Oxide Fuel Cells: Technology Status. Int J Appl Ceram Technol 1(1):5–15. https://doi.org/10.1111/j.1744-7402.2004.tb00149.x
5. Weber A (2021) Fuel Flexibility of Solid Oxide Fuel Cells. Fuel Cells 21(5):440–452. https://doi.org/10.1002/fuce.202100037
6. Hsiao Y (1997) The Degradation of SOFC Electrodes. Solid State Ion 98(1–2):33–38. https://doi.org/10.1016/S0167-2738(97)00106-9
7. Tse ECM, Gewirth AA (2015) Effect of Temperature and Pressure on the Kinetics of the Oxygen Reduction Reaction. J Phys Chem A 119(8):1246–1255. https://doi.org/10.1021/acs.jpca.5b00572
8. Sarapuu A, Kibena-Põldsepp E, Borghei M, Tammeveski K (2018) Electrocatalysis of Oxygen Reduction on Heteroatom-Doped Nanocarbons and Transition Metal–Nitrogen–Carbon Catalysts for Alkaline Membrane Fuel Cells. J Mater Chem A 6(3):776–804. https://doi.org/10.1039/C7TA08690C
9. Ni N, Wang CC, Jiang SP, Skinner SJ. (2019) Synergistic Effects of Temperature and Polarization on Cr Poisoning of $La_{0.6}Sr_{0.4}Co_{0.2}Fe_{0.8}O_{3-\delta}$ Solid Oxide Fuel Cell Cathodes. J Mater Chem A 7(15):9253–9262. https://doi.org/10.1039/C9TA01275C
10. Sakai N, Horita T, Yamaji K, Brito ME, Yokokawa H, Kawakami A, Matsuoka S, Watanabe N, Ueno A (2006) Interface Stability among Solid Oxide Fuel Cell Materials with Perovskite Structures. J Electrochem Soc 153(3):A621. https://doi.org/10.1149/1.2165770
11. Mulmi S, Thangadurai VA (2019) Perovskite-Type $Nd_{0.75}Sr_{0.25}Co_{0.8}Fe_{0.2}O_{3-\delta}$ Cathode for Advanced Solid Oxide Fuel Cells. Chem Commun 55(26):3713–3716. https://doi.org/10.1039/C9CC01054H
12. Hong T, Chen F, Xia C (2015) Barium Carbonate Nanoparticle as High Temperature Oxygen Reduction Catalyst for Solid Oxide Fuel Cell. Electrochem Commun 51:93–97. https://doi.org/10.1016/j.elecom.2014.12.017
13. Jin F, Xu H, Long W, Shen Y, He T (2013) Characterization and Evaluation of Double Perovskites LnBaCoFeO 5+δ (Ln = Pr and Nd) as Intermediate-Temperature Solid Oxide Fuel Cell Cathodes. J Power Sources 243:10–18. https://doi.org/10.1016/j.jpowsour.2013.05.187
14. Li Q, Thangadurai VA (2010) Comparative 2 and 4-Probe DC and 2-Probe AC Electrical Conductivity of Novel Co-Doped Ce0.9−xRExMo0.1O2.1–0.5x (RE = Y, Sm, Gd; x = 0.2, 0.3). J Mater Chem 20(37):7970. https://doi.org/10.1039/c0jm01324b
15. Tesler AB, Lewin DR, Baltianski S, Tsur Y (2010) Analyzing Results of Impedance Spectroscopy Using Novel Evolutionary Programming Techniques. J Electroceramics 24(4):245–260. https://doi.org/10.1007/s10832-009-9565-z
16. Hershkovitz S, Baltianski S, Tsur Y (2011) Harnessing Evolutionary Programming for Impedance Spectroscopy Analysis: A Case Study of Mixed Ionic-Electronic Conductors. Solid State Ion 188(1):104–109. https://doi.org/10.1016/j.ssi.2010.10.004
17. https://Electroceramics.Net.Technion.Ac.Il/Isgp/. Accessed 2 Feb 2023
18. Hershkovitz S, Tomer S, Baltianski S, Tsur Y (2011) ISGP: Impedance Spectroscopy Analysis Using Evolutionary Programming Procedure. ECS Trans 33(40):67–73. https://doi.org/10.1149/1.3589186
19. Oz A, Singh K, Gelman D, Thangadurai V Tsur Y (2018) Understanding of Oxygen Reduction Reaction on Perovskite-Type $Ba_{0.5}Sr_{0.5}Fe_{0.91}Al_{0.09}O_{3-\delta}$ and $Ba_{0.5}Sr_{0.5}Fe_{0.8}Cu_{0.2}O_{3-\delta}$ Using AC Impedance Spectroscopy Genetic Programming. J Phys Chem C 122(27):15097–15107. https://doi.org/10.1021/acs.jpcc.8b03036
20. Toby BH, Von Dreele RB (2013) GSAS-II : The Genesis of a Modern Open-Source All Purpose Crystallography Software Package. J Appl Crystallogr 46(2):544–549. https://doi.org/10.1107/S0021889813003531
21. Momma K, Izumi F (2011) VESTA 3 for Three-Dimensional Visualization of Crystal, Volumetric and Morphology Data. J Appl Crystallogr 44(6):1272–1276. https://doi.org/10.1107/S0021889811038970
22. Lyagaeva J, Danilov N, Tarutin A, Vdovin G, Medvedev D, Demin A, Tsiakaras P (2018) Designing a Protonic Ceramic Fuel Cell with Novel Electrochemically Active Oxygen Electrodes Based on Doped $Nd_{0.5}Ba_{0.5}FeO_{3-\delta}$. Dalton Trans 47(24):8149–8157. https://doi.org/10.1039/C8DT01511B
23. Donazzi A, Pelosato R, Cordaro G, Stucchi D, Cristiani C, Dotelli G, Sora IN (2015) Evaluation of Ba Deficient NdBaCo2O5+δ Oxide as Cathode Material for IT-SOFC. Electrochim Acta 182:573–587. https://doi.org/10.1016/j.electacta.2015.09.117
24. Chang BY (2020) Conversion of a Constant Phase Element to an Equivalent Capacitor. J Electrochem Sci Technol 11(3):318–321. https://doi.org/10.33961/jecst.2020.00815
25. Navarrete L, Solís C, Serra JM (2015) Boosting the Oxygen Reduction Reaction Mechanisms in IT-SOFC Cathodes by Catalytic Functionalization. J Mater Chem A 3(32):16440–16444. https://doi.org/10.1039/C5TA05187H
26. Adler SB (1998) Mechanism and Kinetics of Oxygen Reduction on Porous La1−Sr CoO3− Electrodes. Solid State Ion 111(1–2):125–134. https://doi.org/10.1016/S0167-2738(98)00179-9
27. Boukamp BA (1995) A Linear Kronig-Kramers Transform Test for Immittance Data Validation. J Electrochem Soc 142(6):1885. https://doi.org/10.1149/1.2044210

28. Schönleber M, Klotz D, Ivers-Tiffée E (2014) A Method for Improving the Robustness of Linear Kramers-Kronig Validity Tests. Electrochim Acta 131:20–27. https://doi.org/10.1016/j.electacta.2014.01.034
29. Schönleber M, Ivers-Tiffée E (2015) Approximability of Impedance Spectra by RC Elements and Implications for Impedance Analysis. Electrochem Commun 58:15–19. https://doi.org/10.1016/j.elecom.2015.05.018
30. Boukamp B (2004) Electrochemical Impedance Spectroscopy in Solid State Ionics: Recent Advances. Solid State Ion 169(1–4):65–73. https://doi.org/10.1016/j.ssi.2003.07.002
31. Gill S, Kannan R, Maffei N, Thangadurai V (2013) Effect of Zr Substitution for Ce in BaCe0.8Gd0.15Pr0.05O3−δ on the Chemical Stability in CO2 and Water, and Electrical Conductivity. RSC Adv 3(11):3599
32. Muhammed Ali SA, Anwar M, Ashikin N, Muchtar A, Somalu MR (2018) Influence of Oxygen Ion Enrichment on Optical, Mechanical, and Electrical Properties of LSCF Perovskite Nanocomposite. Ceram Int 44(9):10433–10442. https://doi.org/10.1016/j.ceramint.2018.03.060
33. Jun A, Yoo S, Gwon O, Shin J, Kim G (2013) Thermodynamic and Electrical Properties of Ba0.5Sr0.5Co0.8Fe0.2O3− and La0.6Sr0.4Co0.2Fe0.8O3− for Intermediate-Temperature Solid Oxide Fuel Cells. Electrochimica Acta 89:372–376. https://doi.org/10.1016/j.electacta.2012.11.002.
34. Zurlo F, Di Bartolomeo E, D'Epifanio A, Felice V, Natali Sora I, Tortora L, Licoccia S (2014) La0.8Sr0.2Fe0.8Cu0.2O3− as "Cobalt-Free" Cathode for La0.8Sr0.2Ga0.8Mg0.2O3− Electrolyte. J Power Source 271:187–194. https://doi.org/10.1016/j.jpowsour.2014.07.183
35. Shao Z, Haile SM (2004) A High-Performance Cathode for the next Generation of Solid-Oxide Fuel Cells. Nature 431(7005):170–173. https://doi.org/10.1038/nature02863
36. Cheng Y, Zhou Q, Li W, Wei T, Li Z, An D, Tong X, Ji Z, Han X (2015) Ba0.9Sr0.1Co0.9In0.1O3− Perovskite as Cathode Material for IT-SOFC. J Alloys Compd 641:234–237. https://doi.org/10.1016/j.jallcom.2015.03.257
37. Huang S, Gao F, Meng Z, Feng S, Sun X, Li Y, Wang C (2014) Bismuth-Based Pervoskite as a High-Performance Cathode for Intermediate-Temperature Solid-Oxide Fuel Cells. ChemElectroChem 1(3):554–558. https://doi.org/10.1002/celc.201300070
38. Cascos V, Troncoso L, Alonso JA (2015) New Families of Mn+-Doped SrCo1−xMxO3−δ Perovskites Performing as Cathodes in Solid-Oxide Fuel Cells. Int J Hydrog Energy 40(34):11333–11341. https://doi.org/10.1016/j.ijhydene.2015.03.134
39. Wang F, Zhou Q, He T, Li G, Ding H (2010) Novel SrCo1−yNbyO3−δ Cathodes for Intermediate-Temperature Solid Oxide Fuel Cells. J Power Sources 195(12):3772–3778. https://doi.org/10.1016/j.jpowsour.2009.12.081